KeAi
CHINESE ROOTS
GLOBAL IMPACT

Available online at www.keaipublishing.com/en/journals/journal-of-magnesium-and-alloys/

ScienceDirect

Journal of Magnesium and Alloys 13 (2025) 2295–2306

www.elsevier.com/locate/jma

Full Length Article

First-principles calculations to investigate the structural, elastic and thermodynamic properties of full-Heusler $MgXY_2$ (X = Zn, Cd, Y = Ag, Au, Cu) compounds

Tahsin Özer[a], Murat Çanlı[b,*], Nihat Arıkan[c], Ali İhsan Öztürk[d]

[a] *Osmaniye Korkut Ata University, Bahçe Vocational High School, Osmaniye, , Türkiye*
[b] *Kırşehir Ahi Evran University, Mucur Vocational School, Kırşehir, Türkiye*
[c] *Osmaniye Korkut Ata University, Vocational School of Health Services, Osmaniye, Türkiye*
[d] *Department of Chemistry, Osmaniye Korkut Ata University, Faculty of Science and Letters, Osmaniye, Türkiye*

Received 27 December 2024; received in revised form 6 March 2025; accepted 13 March 2025
Available online 2 April 2025

Abstract

Magnesium and its compounds are recognized as favorable materials for structural uses, primarily due to their lightweight nature and remarkable specific strength. This research employed first-principles methodologies to investigate how pressure affects the crystal structure along with the elastic and thermodynamic characteristics of $MgXY_2$ (X=Zn, Cd, and Y= Ag, Au, Cu) compounds. All analyses were implemented via the Perdew-Burke-Ernzerhof variant of the Generalized Gradient Approximation alongside a plane-wave ultrasoft pseudopotential approach. The findings on the elastic constants indicated that these $MgXY_2$ compounds have maintained their stability at pressures up to 500 kBar. These constants informed detailed assessments of properties like elastic modulus, Poisson's ratio, Vickers hardness, and material anisotropy. The Quantum Espresso software was utilized to calculate melting points, Debye temperature, and minimum thermal conductivity values. A temperature range spanning from 0 to 800 K allowed for an evaluation of vibrational energy, free energy, entropy, and specific heat capacity metrics. The anticipated physical attributes suggest significant potential for these magnesium compounds in biomedical fields.

Keywords: Heusler; Elastic properties; Mechanical properties; Thermodynamic properties; Quantum espresso.

1. Introduction

Global demands for lighter materials continue to rise due to environmental concerns; ongoing studies focus on optimizing microstructural features within magnesium compounds to enhance their performance metrics across diverse applications.

Magnesium is the lightest structural metal, making it an alternative option for applications such as in aerospace and automotive industries where weight reduction is critical. Magnesium and its compounds have excellent biocompatibility because its low density (1.74–1.84 g/ml) and high elasticity (41–45 GPa) are very close to human bone. Magnesium compounds can be classified into two primary groups: wrought and cast compounds, each exhibiting distinct mechanical properties and processing characteristics. Compared to other metals, magnesium compounds are being used as biodegradable and continues to degrade as the bone tissue heals, requiring no second surgery to remove it [1]. Since its Young's modulus value is close to that of cortical bone, it reduces the stress on the bone during the surgery [2,3]. Recent advancements in the development of biodegradable magnesium compounds have sparked interest for medical applications such as scaffolds for bone tissue engineering [4] such as orthopedic biodegradable implants [5,6], high entropy alloys [7] and hydrogen storage products [8] because of their high temperature creep resistance, hydrogen capacity and low den-

* Corresponding author.
E-mail address: murat.canli@ahievran.edu.tr (M. Çanlı).

https://doi.org/10.1016/j.jma.2025.03.012

sity, beside their capacity about strength, stiffness, endurance against magnetism etc. [9–11].

The unique combination of low density and high specific strength makes magnesium compounds an ideal candidate for lightweighting initiatives aimed at improving fuel efficiency in transportation sectors. The addition of alloying elements such as aluminum, zinc, manganese, and rare earth metals significantly enhances the mechanical performance of magnesium-based materials. Several research efforts have extensively tried including rare earth elements to overcome their limitations [3,12,13] such as corrosion and poor mechanical properties that can be used for reducing the anodic effect, followed by the production of sufficient grain size and intermetallic precipitates [14].

Experimental approaches frequently involve complementary information to provide detailed information about the underlying corrosion mechanisms at the atomic level. Ab initio computations are a very promising method of gaining more insight into the fundamental calculations of Mg compounds. Theoretical calculation methods like density functional theory (DFT) have some superior benefits in terms of cost, time, and manpower. Ab initio studies, grounded in quantum mechanics, provide a fundamental understanding of the electronic structure and properties of magnesium compounds, enabling precise predictions of their behavior at the atomic level. DFT as widely used computational approach within ab initio methods allows researchers to effectively model the complex interactions between alloying elements and magnesium's crystal lattice [15]. By leveraging DFT in ab initio studies, scientists can gain insights into phase stability, mechanical properties, and corrosion resistance of magnesium compounds, thereby informing their design for specific applications [16]. Elastic properties also have a great impact on understanding the nature of solid materials [17].

Considering the importance of magnesium compounds in commercial industry applications, in this study, the first-principles calculations were performed on the structural, mechanical, and thermodynamic properties of $MgXY_2$ alloy (X=Zn, Cd, Y=Ag, Au, Cu) to provide new insights about its potential. Nevertheless, this study has investigated the effect of pressure on those properties mentioned above (structural, mechanical and thermodynamic), and the effect of temperature on vibration energy, free energy, entropy, and specific heat capacity was also evaluated.

2. Material and method

Computational details were calculated considering DFT for simulating the elastic and structural properties. In this study, as a software with open-source distribution of computer codes, Quantum ESPRESSO (QE) was chosen to perform all first principle calculations [18]. Ion core interactions with valence electrons were represented by plane-wave (PAW) type pseudo potential files. The potential files were gathered from the software's website. The valence electron configurations are Mg([Ne]$3s^2$), Zn ([Ar]$3d^{10}$ $4s^2$), Cd ([Kr]$4d^{10}$ $5s^2$), Cu ([Ar]$3d^{10}$ $4s^1$), Ag ([Kr]$4d^{10}$ $5s^1$) and Au ([Xe]$4f^{14}$ $5d^{10}$ $6s^1$).

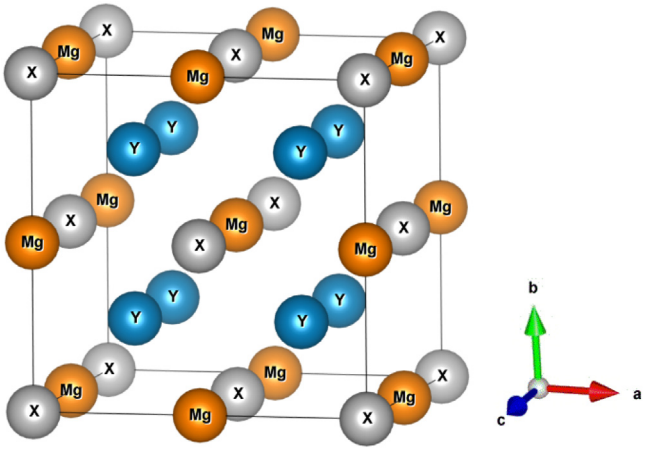

Fig. 1. Crystal structure of $MgXY_2$ alloys.

The Perdew-Burke-Ernzerhof (PBE) version of the Generalized Gradient Approach [19] and the plane-wave ultrasoft pseudopotential method [20] were used in the calculations. PBE is a standard method for gradient-dependent functionals in solid-state physics [21]. The plane-wave ultrasoft pseudopotential allows us to minimize the cutoff energy in calculations while understanding the connection on the electrostatic interactions among ionic cores and valence electrons [22]. After the convergence tests, the k-point and cut-off energy in the Brillouin region were 12 × 12 × 12, 50 Ry, respectively. The lowest energy and ground state of the crystal structure was found for the geometry optimization with the Broyden-Fletcher-Goldfarb-Shannon (BFGS) method [23] under the convergence threshold 1×10^{-4} Ry on the total energy, while convergence threshold 1×10^{-3} Ry was preferred on the forces for ionic minimization.

Thermo_pw code distributed with the QE package was used to calculate elastic constants and the temperature dependence of thermodynamic properties (free energy, vibrational energy, entropy, and heat capacity). In the calculation of thermodynamic properties, the Debye model was preferred within the framework of the Quasi-harmonic approach, and the volume-conserved method was preferred in the calculation of elastic constants.

There are 16 atoms in the $MgXY_2$ alloys that crystallize in the $Fm\bar{3}m$ (225) space group in the cubic crystal system, of which X atoms are 4a (0 0 0), Mg atoms 4b (½ 0 0), Z atoms 8c (¼ ¾ ¾) Wyckoff they are in atomic positions (Fig. 1). The Mg atom is bonded to eight equivalent Y atoms in a body-centered cubic geometry. Mg - Y bond length is 2.78 Å ($MgZnAg_2$,), 2.77 Å ($MgZnAu_2$), 2.87 Å ($MgCdAu_2$), 2.87 Å ($MgCdAg_2$). Y atom is bonded to four equivalents of Mg and four equivalents of X atoms in a body-centered cubic geometry. The X - Y bond length is 2.78 Å ($MgZnAg_2$,), 2.77 Å ($MgZnAu_2$), 2.87 Å ($MgCdAu_2$), 2.88 Å($MgCdAg_2$). The X atom is connected to eight equivalent Y atoms in a distorted body-centered cubic geometry [24].

Table 1
Calculated lattice parameters and elastic constants of $MgXY_2$ alloys between 0 and 500 kBar hydrostatic pressure (a *in Å* and C_{ij} in *GPa*).

P (kBar)	a	$MgZnAg_2$			a	$MgZnAu_2$			a	$MgZnCu_2$		
		C_{11}	C_{12}	C_{44}		C_{11}	C_{12}	C_{44}		C_{11}	C_{12}	C_{44}
0[c]	6.47	81.7	70.1	60.2	6.48	103.4	95.2	55.0	6.06	107.7	90.2	77.8
0	6.42[a], 6.49[b]	79[a]	75[a]	52[a]	6.41[a], 6.48[b]				6.00[b]			
100[c]	6.28	136.6	115.7	84.1	6.30	164.2	148.1	81.4	5.89	147.9	121.5	105.1
200[c]	6.14	190.2	160.0	105.4	6.18	215.0	190.5	103.4	5.77	211.7	176.5	129.4
300[c]	6.03	231.1	191.8	124.6	6.08	241.9	209.3	123.0	5.67	254.5	210.7	150.5
400[c]	5.95	288.0	239.9	142.7	6.01	306.6	266.1	141.5	5.59	279.6	227.4	170.3
500[c]	5.88	330.4	273.8	159.6	5.94	353.3	304.9	158.8	5.53	296.9	236.7	189.2
	a	$MgCdAg_2$			a	$MgCdAu_2$			A	$MgCdCu_2$		
		C_{11}	C_{12}	C_{44}		C_{11}	C_{12}	C_{44}		C_{11}	C_{12}	C_{44}
0[c]	6.70	74.0	67.9	55.5	6.69	96.0	91.5	51.3	6.33	88.5	75.7	68.2
0	6.65[a], 6.63[b]	79	65	48	6.64[a], 6.66[b]				6.20[b]			
100[c]	6.48	129.6	119.3	78.1	6.50	140.1	134.5	74.6	6.12	135.1	116.9	94.0
200[c]	6.33	178.8	163.9	98.1	6.37	190.5	181.4	93.5	5.99	185.7	162.8	113.6
300[c]	6.22	212.2	193.8	115.4	6.27	237.5	224.8	112.0	5.88	232.7	205.8	131.1
400[c]	6.13	230.7	208.6	131.8	6.19	291.7	275.7	128.4	5.80	261.2	230.3	148.5
500[c]	6.05	314.5	289.3	147.5	6.12	333.0	313.9	142.9	5.73	327.4	293.1	163.7

[a] [24]
[b] [25,26].
[c] The values for this work.

3. Findings and discussion

3.1. Structural properties

As a first step, the lattice constants of the $MgXY_2$ alloys between the 0 and 500 kBar pressure range were determined by structural optimization. Table 1 displays the comparison between the determined lattice constants and the literature data available. The data obtained at ambient pressure (0 kBar) are compatible with literature. The empirical relations obtained by fitting a third-order polynomial with MATLAB software at a 95% confidence interval are given below to easily/fastly estimate the lattice constants at the desired intermediate pressure values. In the equation provided, "P" represents the pressure measured in kBar, while "a" denotes the lattice constant expressed in Å. The empirical relations given in Eq. (1) and the values obtained for $P = 0$ is very close to the values given in Table 1. The calculated lattice parameters of $MgZnAg_2$ are 6.47 Å for this study and 6.42 Å and 6.49 Å for literature. Similarly, $MgZnAu_2$ has close values for this study and the literature, 6.48 Å, 6.41 Å and 6.48 Å, respectively. In addition, $MgZnCu_2$, $MgCdAu_2$, $MgCdAg_2$, and $MgCdCu_2$ correspond well with the lattice values of the literature at 0 kBar of P. Thus, it is seen that the empirical relations are compatible with the DFT calculations.

With the effect of applied external pressure or temperature, materials can undergo phase transition. To observe the phase change of the $MgXY_2$ alloys at the working pressures, the V/V_0 graph is drawn as a function of the pressure and is given in Fig. 2. It is seen from Fig. 2 that the $MgXY_2$ alloys do not incur any phase transition at the working conditions.

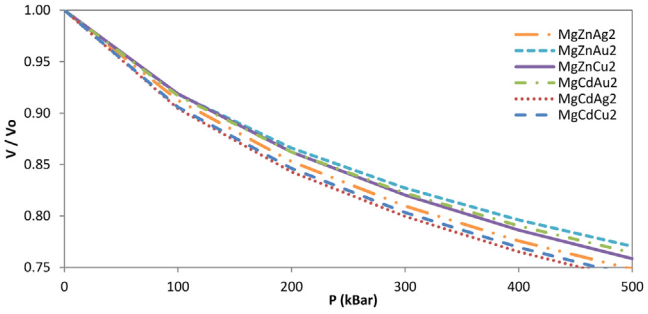

Fig. 2. V/V_o plot as a function of pressure to observe the Phase change of $MgXY_2$ alloys.

The highest resistance to pressure was exhibited by $MgZnAu_2$ (over 500 kBar) while the lowest resistance was detected in $MgCdAg_2$ (around 450 kBar).

3.2. Elastic properties

Structural, thermal, and mechanical behaviors lean on elastic properties. Table 1 examines three elastic constants independent of the cubic phase, C_{11}, C_{12}, and C_{44}, in comparison with the available literature. These elastic constants meet the criteria for elastic stability ($C_{44}>0$, $C_{11} > |C_{12}|$, $C_{11}+2C_{12}>0$) of cubic crystals in the Born-Huang stability criterion [27]. The stability criteria also lead to a limitation in the size of the bulk modulus B ($C_{12}<B < C_{11}$) [28]. Providing the Born-Huang stability criterion also makes the $MgXY_2$ alloys mechanically stable. In addition, the values calculated at ambient pressure are consistent with the literature as hav-

Table 2
Elastic properties measured in GPa, along with the Poisson's ratio.

P (kBar)	$MgZnAg_2$							$MgZnAu_2$					
	Ref.	B	G_H	G_H/B_H	E_H	ϑ_H	C_P	B	G_H	G_H/B_H	E_H	ϑ_H	C_P
0	[a]	74.0	25.5	0.35	68.7	0.345	10.0	97.9	21.9	0.22	61.2	0.396	40.2
0	[b]	76	18			0.39							
100		122.6	38.3	0.31	104.1	0.359	31.6	153.5	34.8	0.23	97.1	0.395	66.7
200	[a]	170.1	50.2	0.29	137.0	0.366	54.6	198.7	46.5	0.23	129.3	0.392	87.1
300	[a]	204.9	61.2	0.30	166.9	0.364	67.2	220.1	57.2	0.26	157.8	0.380	86.2
400	[a]	256.0	71.6	0.28	196.5	0.372	97.2	279.6	67.3	0.24	187.0	0.389	124.6
500	[a]	292.7	81.5	0.28	223.7	0.373	114.2	321.1	77.1	0.24	214.1	0.389	146.1
	$MgZnCu_2$							$MgCdAg_2$					
	Ref.	B	G_H	G_H/B_H	E_H	ϑ_H	C_P	B	G_H	G_H/B_H	E_H	ϑ_H	C_P
0	[a]	96.1	34.4	0.36	92.3	0.340	12.4	69.9	20.8	0.30	56.9	0.364	12.3
0	[b]							69	23			0.35	
100	[a]	130.3	48.0	0.37	128.4	0.336	16.4	122.7	30.3	0.25	84.1	0.386	41.2
200	[a]	188.2	60.6	0.32	164.2	0.355	47.1	168.8	39.3	0.23	109.3	0.392	65.8
300	[a]	225.3	72.0	0.32	195.1	0.356	60.3	199.9	46.8	0.23	130.1	0.391	78.4
400	[a]	244.8	82.8	0.34	223.3	0.348	57.1	216.0	54.0	0.25	149.6	0.385	76.8
500	[a]	256.8	93.1	0.36	249.2	0.338	47.5	297.7	60.7	0.20	170.6	0.405	141.8
	$MgCdAu_2$							$MgCdCu_2$					
	Ref.	B	G_H	G_H/B_H	E_H	ϑ_H	C_P	B	G_H	G_H/B_H	E_H	ϑ_H	C_P
0	[a]	93.0	18.5	0.20	52.0	0.407	40.2	80.0	28.7	0.36	76.9	0.340	7.5
100	[b]	136.3	26.3	0.19	74.0	0.410	59.9	123.0	39.9	0.32	108.1	0.354	22.9
200	[a]	184.4	34.3	0.19	96.8	0.413	87.8	170.4	48.8	0.29	133.7	0.369	49.2
300	[a]	229.0	42.1	0.18	119.1	0.413	112.9	214.7	56.6	0.26	156.1	0.379	74.6
400	[a]	281.1	49.2	0.18	139.6	0.417	147.4	240.6	64.3	0.27	177.2	0.377	81.8
500	[a]	320.3	55.7	0.17	157.9	0.418	171.0	304.5	71.1	0.23	197.9	0.392	129.3

[a] The values of this work.
[b] [24].

ing 8.8% difference for $MgCdAg_2$ and 8.5% difference for $MgZnAg_2$ on average from the values reported by Jain et al. [24].

At 0–500 kBar pressure, C_{11}, C_{12} and C_{44} values increased by 304.4%, 290.5%, 165.3% in $MgZnAu_2$ alloy, by 241.7%, 220.4%, 188.9% in $MgZnAg_2$ alloy, by 175.6%, 162.4%, 143.2% in $MgZnCu_2$ alloy, by 324.7%, 326.3%, 165.7% in $MgCdAg_2$ alloy, by 246.8%, 242.9%, 178.4% in $MgCdAu_2$ alloy, by 270.1%, 287.1%, 140.2% in $MgCdCu_2$ alloy, respectively. Pressure sensitivity of alloys $MgCdAg_2$ > $MgZnAg_2$ > $MgCdAu_2$ > $MgZnAu_2$ > $MgCdCu_2$ > $MgZnCu_2$. The most change has been in the $MgCdAg_2$ alloy. In this state, $MgCdAg_2$ alloys are more pressure sensitive than other alloys. For this reason, $MgCdAg_2$ alloys can be preferred in applications requiring pressure sensitivity.

Bulk modulus B, Young's modulus E, shear modulus G, Poisson's ratio ϑ, and Cauchy pressure (C_p=C_{12}-C_{44}) were calculated with using the elastic constants in Table 1, and their variations against pressure are given in Table 2 and Fig. 3. G denotes the resistance level to plastic deformation and calculated with G_V and G_R in Eq. (2). G_V (the Voigt shear modulus) and G_R (the Reuss shear modulus) are used for the calculation of G. With moving pressure from 0 to 500 kbar, $MgXY_2$'s elastic constants and mechanical modulus are higher. This indicates that more external forces are required to compress the alloys.

$$B_V = B_R = (C_{11} + 2C_{12})/3 \tag{1}$$

$$G_V = \frac{C_{11} - C_{12} + 3C_{44}}{5}$$
$$G_R = \frac{5(C_{11} - C_{12})C_{44}}{4C_{44} + 3(C_{11} - C_{12})} \quad G = \frac{G_R + G_V}{2} \tag{2}$$

$$E_X = \frac{9B_X G_X}{G_X + 3B_X} \tag{3}$$

$$\vartheta_X = \frac{1}{2}\left[\frac{B_X - (2/3)G_X}{B_X + (1/3)G_X}\right] \tag{4}$$

The values calculated for $P = 0$ with Eqs. (6)-11 is on average 0.21% ($MgZnAg_2$), 0.32% ($MgZnAu_2$), 0.85% ($MgZnCu_2$), 1.62% ($MgCdAg_2$), 0.12% ($MgCdAu_2$), 0.87 ($MgCdCu_2$) is different from the values given in Table 3. These equations are consistent with the data shown in Table 3. The pressure derivative of the bulk modulus was calculated as $B_0'(dB_0/dP)$, 0.5 ($MgZnAg_2$), 0.6 ($MgZnAu_2$), 0.4 ($MgZnCu_2$), 0.9 ($MgCdAg_2$), 0.4 ($MgCdAu_2$), 0.6 ($MgCdCu_2$). Due to the low Bulk modulus and derivative of the Bulk modulus of the $MgXY_2$ alloys, it shows that this material will not suddenly harden as the pressure increases.

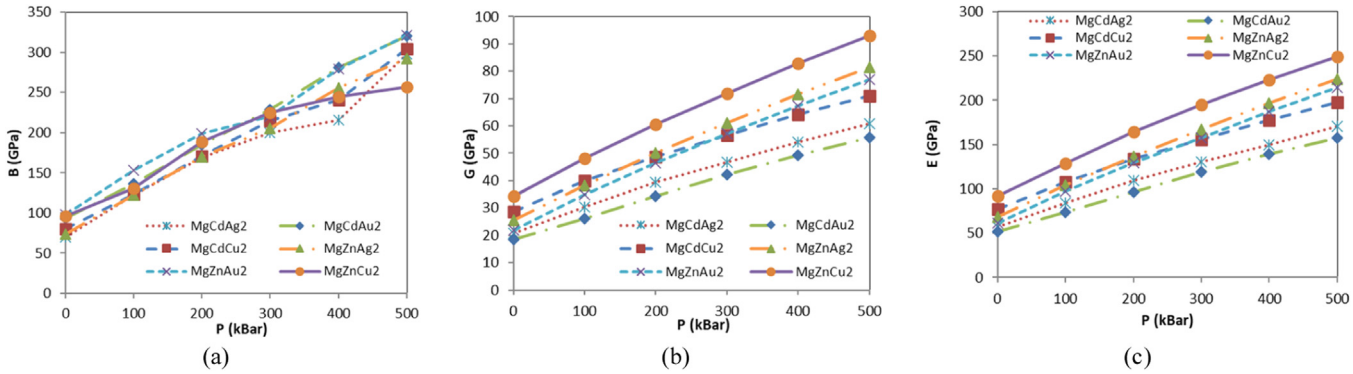

Fig. 3. Graph of the variation of B, G and E with pressure for $MgXY_2$ alloy.

Table 3
Density ρ (kg/m^3), Debye temperature θ_D (K), longitudinal υ_l (m/s), transverse υ_s (m/s), and sound velocity υ_m (m/s), Anisotropy factors and Vicker hardness.

P (kBar)		υ_s	υ_l	υ_m	θ_D	ρ	A^U	A_Z	ζ	H^a	H^b
0	$MgZnAg_2$	1847.5	3799.7	2075.8	240.6	7481.9	10.2	10.4	0.90	2.64	2.722
	$MgZnAu_2$	1363.3	3283.0	1542.4	178.5	11,796.2	13.8	13.4	0.95	1.52	1.494
	$MgZnCu_2$	2307.1	4684.2	2590.4	320.7	6470.9	8.4	8.9	0.89	3.68	3.512
	$MgCdAg_2$	1635.9	3542.2	1842.9	206.4	7787.4	19.2	18.0	0.94	1.88	1.995
	$MgCdAu_2$	1253.6	3162.9	1420.4	159.3	11,764.3	25.1	22.8	0.97	1.15	1.156
	$MgCdCu_2$	2038.2	4136.0	2288.4	271.3	6912.6	10.5	10.7	0.90	3.07	3.094
100	$MgZnAg_2$	2161.5	4602.8	2433.0	290.7	8199.4	7.4	8.0	0.89	3.61	3.238
	$MgZnAu_2$	1646.6	3944.9	1862.6	221.8	12,845.1	9.8	10.1	0.93	2.45	2.105
	$MgZnCu_2$	2611.8	5253.3	2930.9	373.2	7043.1	7.3	8.0	0.88	5.26	4.588
	$MgCdAg_2$	1876.8	4353.1	2120.5	245.6	8611.1	15.8	15.1	0.95	2.31	2.103
	$MgCdAu_2$	1430.5	3654.5	1621.4	187.1	12,829.5	29.5	26.6	0.97	1.58	1.429
	$MgCdCu_2$	2287.4	4805.3	2572.9	315.2	7631.5	10.1	10.3	0.91	3.90	3.483
200	$MgZnAg_2$	2391.0	5196.9	2694.0	329.3	8772.4	6.1	7.0	0.89	4.49	3.670
	$MgZnAu_2$	1846.8	4374.2	2088.2	253.6	13,621.0	7.9	8.4	0.92	3.36	2.670
	$MgZnCu_2$	2842.0	5987.2	3197.3	415.9	7505.0	6.6	7.3	0.88	5.88	4.639
	$MgCdAg_2$	2061.5	4892.9	2331.1	276.4	9239.4	13.5	13.2	0.94	2.82	2.356
	$MgCdAu_2$	1584.5	4106.3	1796.8	211.7	13,645.4	22.4	20.6	0.97	2.00	1.657
	$MgCdCu_2$	2445.0	5369.7	2756.1	345.4	8168.6	9.6	9.9	0.92	4.26	3.485
300	$MgZnAg_2$	2573.2	5568.4	2898.6	360.5	9240.8	5.4	6.3	0.88	5.54	4.284
	$MgZnAu_2$	2002.2	4558.5	2260.5	278.7	14,261.5	6.8	7.5	0.91	4.56	3.485
	$MgZnCu_2$	3020.5	6381.7	3398.5	449.5	7888.6	6.0	6.9	0.88	6.93	5.189
	$MgCdAg_2$	2191.2	5189.2	2477.6	298.9	9739.4	12.7	12.5	0.94	3.38	2.684
	$MgCdAu_2$	1715.8	4464.6	1945.9	232.9	14,308.7	19.0	17.8	0.96	2.43	1.896
	$MgCdCu_2$	2564.7	5807.2	2894.9	369.2	8605.3	9.4	9.7	0.92	4.57	3.519
400	$MgZnAg_2$	2724.7	6036.3	2792.0	387.6	9645.2	4.9	5.9	0.88	6.11	4.447
	$MgZnAu_2$	2131.9	4993.2	2409.6	300.9	14,815.8	6.1	7.0	0.91	5.00	3.591
	$MgZnCu_2$	3172.6	6570.3	3566.0	478.3	8229.8	5.6	6.5	0.87	8.40	6.120
	$MgCdAg_2$	2303.9	5319.9	2792.0	318.7	10,177.8	12.0	11.9	0.93	4.16	3.207
	$MgCdAu_2$	1818.9	4826.4	2063.9	250.3	14,885.3	16.9	16.1	0.96	2.72	2.004
	$MgCdCu_2$	2676.0	6027.7	3019.9	390.7	8983.9	9.3	9.6	0.92	5.26	3.915
500	$MgZnAg_2$	2854.9	6335.2	3219.6	411.1	9999.3	4.6	5.6	0.88	6.92	4.848
	$MgZnAu_2$	2243.5	5261.2	2535.9	320.2	15,310.9	5.7	6.6	0.91	5.71	3.936
	$MgZnCu_2$	3303.7	6682.0	3708.5	503.4	8531.7	5.3	6.3	0.86	10.04	7.194
	$MgCdAg_2$	2397.9	5988.0	2716.1	336.7	10,560.7	11.8	11.7	0.95	3.87	2.763
	$MgCdAu_2$	1901.7	5062.3	2158.0	264.6	15,393.9	15.6	14.9	0.96	3.05	2.166
	$MgCdCu_2$	2761.6	6544.8	3122.6	408.9	9321.4	9.2	9.5	0.93	5.13	3.602

[a] [29].
[b] [30].

Although data to compare the results obtained are not yet available, it will provide guidance for future experiments.

The variation of *B, G,* and *E* values with pressure is visualized and given in Fig. 3–4. With increasing pressure, $MgXY_2$ alloys showed an approximately linear increase like each other. $MgZnCu_2$ has the highest shear modulus and Young's modulus change while $MgCdAu_2$ shows the bulk modulus value. This increase indicates that *B, G,* and *E* values can be improved under appropriate pressure. In addition, since the size of the *B* and *G* values indicate homologous properties,

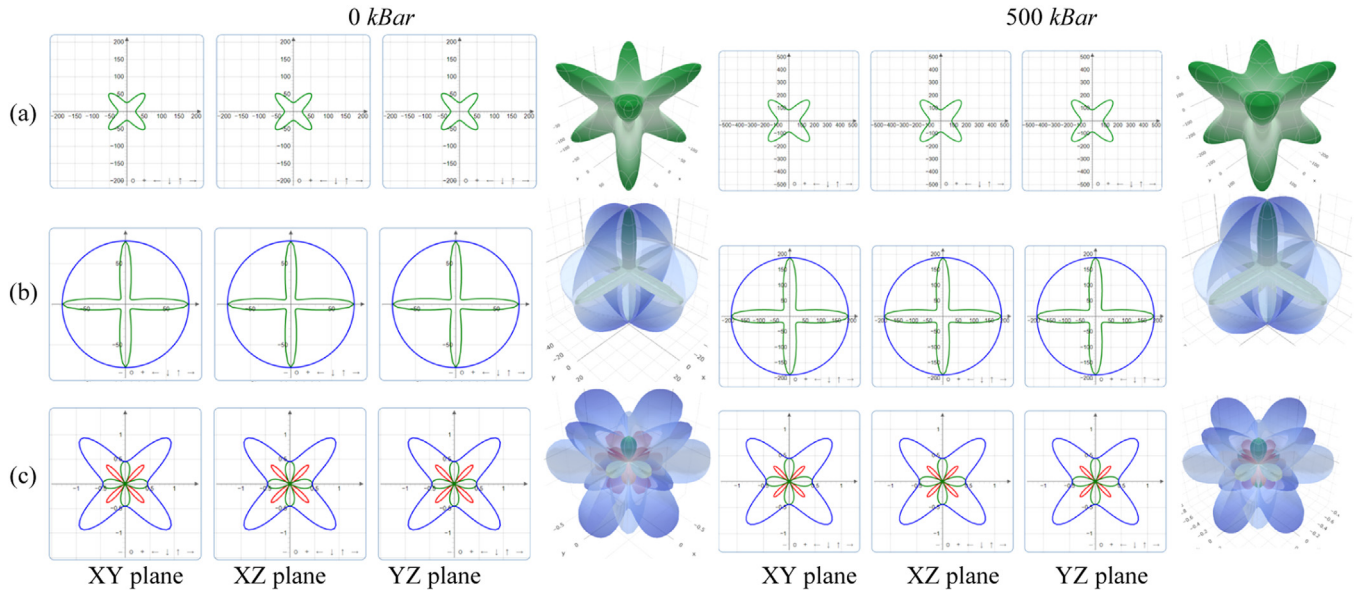

Fig. 4. Two- and three-dimensional representation of Young's modulus (a). Shear modulus (b). Poisson's ratio (c) of $MgZnCu_2$ alloy at ambient and 500 kBar pressure.

the increase in the B and G values means that the homologous property can be improved. Since the E value predicts the hardness of the material better than B and G, the increase in the E value with pressure indicates that the material will become stiffer, in other words, the stiffer property can be improved.

The hardness of $MgXY_2$ alloys can be estimated more accurately by looking at the B, G and E values as well as the Vicker hardness.

$$H_v = \frac{(1-2\vartheta)E}{6(1+\vartheta)} \tag{5}$$

$$H_v = 0.92\, k^{1.137} G^{0.708} \tag{6}$$

The Vicker hardness calculated with the models proposed by Wafula et al. [21] as in Eq. (5) and Tian et al. [30] as in Eq. (6) is given in Table 3 and Fig. 5. The results of both models are consistent with each other and the difference between them is thought to be due to the model difference. $MgZnCu_2$ alloy is a harder material than other alloys (Table 3 and Fig. 5). Increasing pressure caused an increase in Vicker hardness of all the alloys. 10 GPa is a critical level for Vicker hardness, and substances below this value are classified as soft materials, while those above this value are classified as hard materials. Along with this classification, $MgXY_2$ alloys are soft material at working pressures and not suitable for use in applications requiring hardness.

Material can be predicted theoretically as brittle and ductile by looking at its G/B, ϑ and C_p values. The critical value for G/B is 0.57. If it is less than this value, it will behave ductile, otherwise it will behave brittle. $MgXY_2$ alloys will exhibit ductile property since they have G/B ratios less than the critical value of all pressure values studied. The ductile also increased with the increase in pressure. If ϑ is ϑ<0.26, it is brittle, otherwise it is ductile. The ϑ value is greater than the critical value for all alloys and increased with increasing pressure. Again, positive (negative) C_p value indicates the ductile (brittle) nature of the material. The C_p value was positive for all alloys and this value increased with the increase in pressure. The judgment reached by all three criteria (G/B, ϑ and C_p) is consistent with each other and increases the reliability of the calculation.

The Poisson ratio, known as the transverse deformation coefficient, reflects the strength of the covalent bond. Generally, if the ϑ ratio is 0.1∼0.28, the material shows covalent properties, and if it is greater than 0.29, it exhibits metallic properties [31,32]. Since the calculated ϑ>0.29, the $MgXY_2$ alloy is metallic.

The Kleinman parameter (ζ) represents bending and stretching nature of bonds. It is dimensionless and takes values between 0 and 1, and calculated with Eq. (7) [21,33]. The lower limit of ζ corresponds to the minimized bending bond while the higher limit agrees with the minor stretching bond contribution.

$$\zeta = \frac{C_{11}+8C_{12}}{7C_{11}+2C_{12}} \tag{7}$$

As can be seen from this equation, the ζ parameter depends on the values of C_{11} and C_{12}. If C_{11}=C_{12}, ζ reaches the maximum value, that is, ζ=1. The more C_{11} is greater than C_{12}, the closer ζ gets to the minimum value. ζ is close to the maximum value (Table 3). All the alloys have ζ values between 0.86–0.97. In other words, the bonding nature of $MgXY_2$ is expected to be dominated by the bond stretching term.

3.3. Anisotropy of the material

Anisotropy is defined as the physical properties measurable in the material that depend on the crystal direction.

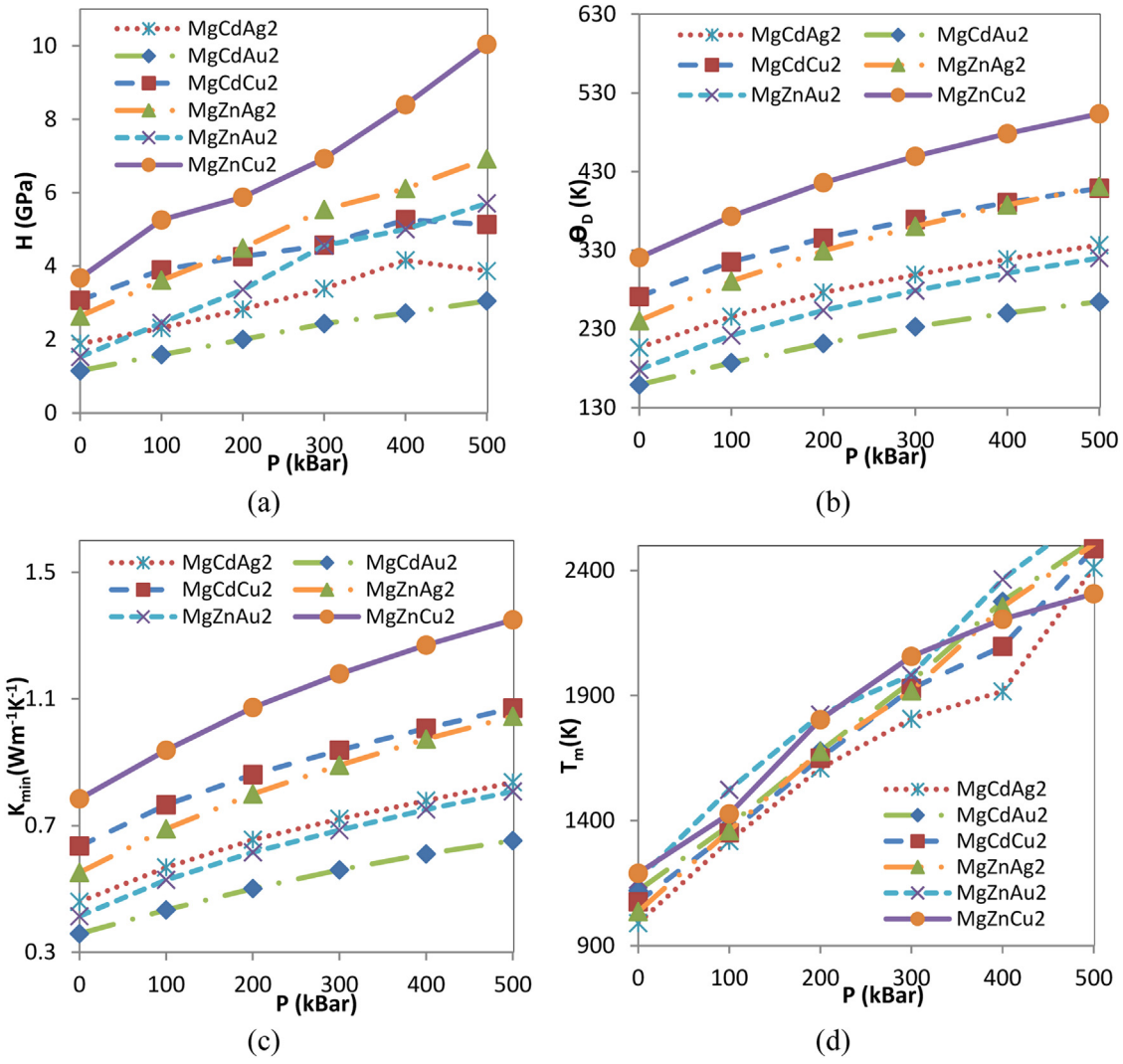

Fig. 5. Effect of Vicker Hardness (a), Debye temperature (b), minimum thermal conductivity (c) and melting temperature (d) with pressure of $MgXY_2$ alloys.

The greater the elastic anisotropy, the easier the formation of microcracks. Microcracks affect material strength. Therefore, the management of microcracks is important to increase material strength. The anisotropy of the elastic modulus can be explained by the assistance of elastic anisotropic index, the three-dimensional (3D) surface structure, and the two-dimensional (2D) projection of the 3D surface structure. For the elastic anisotropic index, the expressions used for the calculation of the Universal anisotropy index (A^U) [34] and the Zener factor (A_Z) [35,36] are given below and the results are shown in Table 3.

$$A^U = 5\frac{G_V}{G_R} + \frac{B_V}{B_R} - 6 \geq 0 \tag{8}$$

$$A_Z = \frac{2C_{44}}{C_{11} - C_{12}} \tag{9}$$

Isotropic materials have the Universal anisotropy index and the Zener factor as A_Z=1 and A^U=0. The degree of anisotropy depends on the deviation from one to zero. Table 3 shows that $MgXY_2$ alloys exhibit anisotropic behavior. However, A_Z and A^U values decreased with increasing pressure. For example, the values of A_z for $MgZnAg_2$ have dropped from 10.4 to 5.6. The dropping percentages of A_z with increasing temperature from 100 to 500 K are 46.15% of $MgZnAg_2$, 50.75% of $MgZnAu_2$, 29.22% of $MgZnCu_2$, 35.00% of $MgCdAg_2$, 34.65% of $MgCdAu_2$, and 11.22% of $MgCdCu_2$. All alloys get close to being isotropic material with increasing temperature. $MgZnAg_2$ is the closest alloy to being isotropic compared to others. Since $B_V = B_R$ in cubic structures, B_V/B_R=1 and will not increase with raising pressure. At the working pressures, the G_V/G_R ratio gets higher with the increase in pressure, and as a result, the A^U values decreased. This reduction indicates that the anisotropic nature of the $MgXY_2$ alloys can be improved.

The anisotropy of the $MgZnCu_2$ alloy is the only alloy visualized with the ELATE software [37], because all other alloys have similar anisotropies (Fig. 5). The maximum value of the shear modulus is isotropic. The anisotropicity of the Young's modulus and the maximum value of the Poisson's ratio decreased with increasing pressure. This shows

Table 4
Transverse and longitudinal sound velocities in crystal directions [100], [110], and [111] in $MgXY_2$ alloy (as m/s).

Comp.	*P (kBar)*	[100]			[110]			[111]		
		$[100]v_l$	$[001]v_{t1}$	$[001]v_{t2}$	$[110]v_l$	$[1\bar{1}0]v_{t1}$	$[001]v_{t2}$	$[111]v_l$	$[112]v_{t1}$	$[11\bar{2}]v_{t2}$
$MgZnAg_2$	0	3305	2836	2836	4265	1245	2836	4540	1788	1788
	100	4081	3202	3202	5063	1596	3202	5350	2065	2065
	200	4656	3466	3466	5654	1855	3466	5950	2269	2269
	300	5001	3673	3673	6031	2062	3673	6337	2432	2432
	400	5465	3847	3847	6494	2232	3847	6802	2568	2568
	500	5748	3995	3995	6795	2380	3995	7110	2685	2685
$MgZnAu_2$	0	2960	2159	2159	3616	834	2159	3810	1336	1336
	100	3576	2518	2518	4301	1121	2518	4516	1591	1591
	200	3973	2755	2755	4741	1341	2755	4970	1769	1769
	300	4118	2937	2937	4944	1512	2937	5190	1907	1907
	400	4549	3090	3090	5374	1654	3090	5622	2023	2023
	500	4803	3221	3221	5645	1777	3221	5899	2124	2124
$MgZnCu_2$	0	4080	3467	3467	5227	1644	3467	5556	2215	2215
	100	4583	3863	3863	5835	1936	3863	6196	2494	2494
	200	5311	4152	4152	6565	2166	4152	6933	2704	2704
	300	5680	4367	4367	6969	2355	4367	7348	2865	2865
	400	5829	4549	4549	7176	2518	4549	7573	3002	3002
	500	5899	4709	4709	7311	2655	4709	7724	3121	3121
$MgCdAg_2$	0	3083	2670	2670	4030	891	2670	4299	1625	1625
	100	3880	3011	3011	4850	1096	3011	5132	1850	1850
	200	4399	3259	3259	5400	1269	3259	5695	2019	2019
	300	4668	3442	3442	5717	1377	3442	6027	2140	2140
	400	4761	3599	3599	5877	1473	3599	6204	2245	2245
	500	5457	3738	3738	6524	1544	3738	6842	2335	2335
$MgCdAu_2$	0	2857	2089	2089	3512	618	2089	3705	1258	1258
	100	3304	2411	2411	4064	661	2411	4287	1443	1443
	200	3736	2618	2618	4526	816	2618	4760	1583	1583
	300	4074	2798	2798	4897	939	2798	5142	1704	1704
	400	4427	2937	2937	5262	1037	2937	5512	1798	1798
	500	4651	3047	3047	5504	1116	3047	5760	1873	1873
$MgCdCu_2$	0	3577	3140	3140	4662	1359	3140	4971	1975	1975
	100	4207	3509	3509	5369	1543	3509	5704	2213	2213
	200	4768	3729	3729	5936	1676	3729	6277	2361	2361
	300	5200	3904	3904	6381	1768	3904	6729	2474	2474
	400	5392	4066	4066	6625	1854	4066	6988	2580	2580
	500	5926	4191	4191	7131	1919	4191	7489	2661	2661

that the isotropic structure can be improved under appropriate pressure. The surface structure of the Young's modulus approaches sphericity with increasing pressure indicates that it has low elastic anisotropy. A^U and A_Z values decreased with increasing pressure (Table 3). The judgment reached by the analysis of the surface structures supports the result reached by the elastic anisotropic index. The results are consistent among themselves.

3.4. Thermal properties

Several physical properties such as elastic constants, thermal conductivity, and melting temperature adjust Debye temperature θ_D to be estimated with the following equations (Eqs. (10)-12).

$$\theta_D = \frac{h}{k_B}\left(\frac{3}{4\pi V_a}\right)^{1/3} v_m \tag{10}$$

$$v_m = \left[\left(\frac{2}{v_s^3} + \frac{1}{v_l^3}\right)/3\right]^{-1/3} \tag{11}$$

$$v_l = \sqrt{(B_x + 4G_x/3)/\rho} \quad v_s = \sqrt{G_x/\rho} \tag{12}$$

Here, k_B, h, V_a, and υ_m correspond to Boltzmann constant, Planck constant, atomic volume, and average sound velocity, respectively. The calculated Debye temperature, transverse and longitudinal sound velocities are given in Table 4. The Debye temperature of the $MgXY_2$ alloys increased with increasing pressure (Table 3). The increased Debye temperature occurs in response to the vibrations of the $MgXY_2$ alloys, which increase when the pressure increases. $MgZnCu_2$ alloy with lower density and larger elastic modules appear to have higher sound velocities and higher Debye temperature than other alloys. A higher Debye temperature reflects stronger bond strength and hardness. As can be seen from Table 3, the highest hardness belongs to $MgZnCu_2$ alloy.

In a cubic crystal, the transverse and longitudinal sound velocities are in three different crystal directions [100], [110], and [111]. Each direction has one longitudinal mode and two transverse modes. All of these modes correspond to the transverse and longitudinal acoustic branches in the phonon spec-

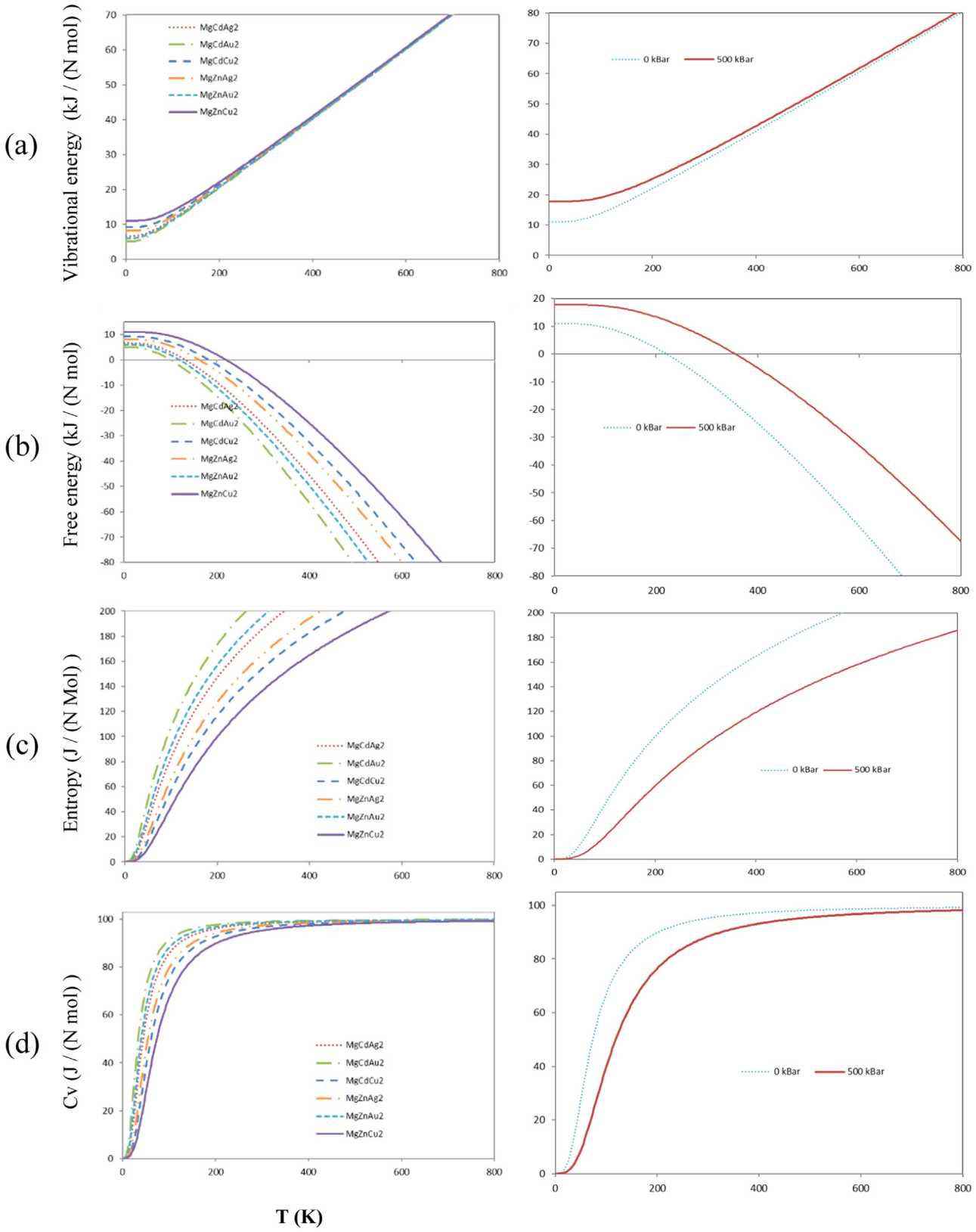

Fig. 6. Free energy (a), Vibrational energy (b), Entropy (c), and Heat capacity (d) of $MgXY_2$ alloy at ambient pressure and 500 kBar. The second graphs belong to the $MgZnCu_2$ alloy.

Table 5
Calculated acoustic Gruneisen constant, thermal conductivity and melting temperature.

Comp.	P (kBar)	M_a	k_{min}(W.m^{-1}.K^{-1})		γ_a	T_m (K)	
		(10^{-25})	Clarke	Cahil		Fine	Özer
$MgZnAg_2$	0	1.27	0.552	0.63	2.092	1035.9	915.8
	100	1.27	0.690	0.80	2.204	1360.0	1177.0
	200	1.27	0.800	0.94	2.269	1677.0	1435.3
	300	1.27	0.891	1.04	2.255	1919.1	1635.6
	400	1.27	0.973	1.15	2.329	2255.2	1911.0
	500	1.27	1.045	1.23	2.334	2505.8	2118.9
$MgZnAu_2$	0	2.01	0.414	0.51	2.577	1164.0	1013.1
	100	2.01	0.528	0.64	2.562	1523.6	1295.6
	200	2.01	0.616	0.75	2.529	1823.7	1536.8
	300	2.01	0.685	0.82	2.412	1982.4	1667.1
	400	2.01	0.751	0.91	2.496	2365.1	1976.6
	500	2.01	0.808	0.98	2.500	2640.8	2201.7
$MgZnCu_2$	0	0.90	0.784	0.90	2.050	1189.6	1037.5
	100	0.90	0.938	1.07	2.019	1427.1	1224.7
	200	0.90	1.073	1.24	2.170	1804.1	1526.2
	300	0.90	1.179	1.36	2.179	2057.0	1731.3
	400	0.90	1.270	1.46	2.115	2205.5	1854.1
	500	0.90	1.350	1.54	2.037	2307.5	1939.5
$MgCdAg_2$	0	1.46	0.459	0.54	2.257	990.6	868.0
	100	1.46	0.568	0.68	2.467	1319.1	1118.3
	200	1.46	0.655	0.80	2.535	1609.4	1342.0
	300	1.46	0.721	0.88	2.528	1807.2	1492.1
	400	1.46	0.779	0.93	2.454	1916.7	1572.6
	500	1.46	0.837	1.04	2.679	2411.6	1959.6
$MgCdAu_2$	0	2.20	0.358	0.45	2.707	1120.6	971.0
	100	2.20	0.433	0.54	2.741	1380.9	1156.7
	200	2.20	0.501	0.63	2.779	1678.6	1384.1
	300	2.20	0.560	0.71	2.790	1956.4	1596.5
	400	2.20	0.610	0.78	2.841	2277.2	1844.9
	500	2.20	0.653	0.84	2.849	2521.2	2033.4
$MgCdCu_2$	0	1.10	0.635	0.72	2.048	1075.8	942.6
	100	1.10	0.765	0.88	2.161	1351.4	1151.0
	200	1.10	0.861	1.01	2.302	1650.7	1383.0
	300	1.10	0.939	1.12	2.395	1928.1	1597.3
	400	1.10	1.007	1.20	2.379	2096.8	1725.2
	500	1.10	1.071	1.30	2.531	2487.8	2031.1

trum [38]. Elastic constants help to find pure longitudinal and transverse waves using the following equations. These equations to express the first couple transverse modes, respectively v_{t1} and v_{t2} [39];

$$[100]v_l = \sqrt{C_{11}/\rho};\ [010]v_{t1} = [001]v_{t2} = \sqrt{C_{44}/\rho} \tag{13}$$

$$[110]v_l = \sqrt{(C_{11} + C_{12} + 2C_{44})/2\rho};$$
$$\left[1\bar{1}0\right]v_{t1} = \sqrt{(C_{11} - C_{12})/\rho};\ [001]v_{t2} = \sqrt{C_{44}/\rho}$$

$$[111]v_l = \sqrt{(C_{11} + 2C_{12} + 4C_{44})/3\rho};$$
$$\left[11\bar{2}\right]v_{t1} = v_{t2} = \sqrt{(C_{11} - C_{12} + C_{44})/3\rho}$$

The transverse and longitudinal sound velocities in the crystal directions of the $MgXY_2$ alloys are calculated and listed in Table 4. As can be clearly seen from the table, the sound velocities in the directions increased with the increase in pressure. However, this increase differs according to the directions. As a result of this difference, the speed of sound is anisotropic. This anisotropic property at sound speeds indicates elastic anisotropy, which confirms the judgment reached by the elastic anisotropic index. Reaching the same conclusion with different approaches increases the reliability of the study.

Greater lattice thermal conductivity and melting temperature help with stronger bond strength and higher hardness, which turns into a higher Debye temperature (Fig. 5, Table 3, and Table 5). A pure crystal has an intrinsic minimum lattice thermal conductivity (k_{min}) with a theoretical lower limit of thermal conductivity [40]. Minimum thermal conductivity [41–45],

$$k_{min} = 0.87\ k_B\ {M_a}^{-2/3}\ E^{1/2}\ \rho^{1/6} \tag{14}$$

$$M_a = [M/(m.N_A)] \tag{15}$$

$$k_{min} = \frac{k_B}{2.48} m^{\frac{2}{3}} (2v_t + v_l) \tag{16}$$

$$\gamma_a = \frac{3}{2}\left(\frac{3v_l^2 - 4v_s^2}{v_l^2 + 2v_s^2}\right) \quad (17)$$

where M, N_A, m, M_a, k_B, and ρ are molecular mass, Avogadro's constant, number of atoms per molecule, average atomic mass, Boltzmann constant, and density of $MgXY_2$, respectively. The k_{min}, calculated with two different models is listed in Table 5. The value of k_{min} increased with increasing pressure because of appropriate pressure exposure. We did not find any data to compare the k_{min} value. The change of k_{min} stayed between 0.358–1.350 $W.m^{-1}.K^{-1}$ [43] and 0.45–1.30 $W.m^{-1}.K^{-1}$ [42] for all $MgXY_2$ alloys. Compared to $Ln_2Zr_2O_7$ (1.2–1.4 $W.m^{-1}.K^{-1}$) and $Ln_2SrAl_2O_7$ (1.49–1.60 $W.m^{-1}.K^{-1}$) [46], $MgXY_2$ has a potential as thermal barrier coating material at ambient pressure.

It is important to know the melting temperature of the material in applications requiring temperature. Melting temperatures can be determined experimentally as well as predicted theoretically. Some of the models that predict the melting temperature using elastic constants are [47,48]:

$$T_m(K) = 553 + 5.91\ C_{11} \quad (18)$$

$$T_m(K) = 560.4\ +\ 7.805\ C_{11} - 3.094\ C_{12} - 1.086\ C_{44} \quad (19)$$

The melting temperatures for both models were calculated and given in Table 5 (Eqs. (18)-19). The melting temperature calculated by the empirical equations proposed by Fine et al. [47] and Özer [48] differs on average by 15%. Since $MgXY_2$ alloys have melting temperatures of over 1000 K, they are potential candidate materials for high temperature applications. The graph drawn as a function of pressure to visualize the effect of pressure on Vicker hardness, Debye temperature, thermal conductivity and melting temperature is given in Fig. 5. $MgZnCu_2$ has the highest increase and top values for Vicker hardness, Debye temperature and thermal conductivity against increasing pressure 0 to 500 kBar among all the $MgXY_2$ alloys (Fig. 5). For melting temperature, $MgZnAu_2$ shows the highest value and increase (around 1000 to over 2400 K).

The vibration energy (Fig. 6a), given as a function of temperature, increases linearly independent of pressure after a temperature of about 300K. Among the $MgXY_2$ alloys, the highest free energy was $MgZnCu_2$ and the lowest $MgCdAu_2$ alloy (Fig. 6b). The free energy of the alloys similarly decreased with increasing temperature. The free energy increased with increasing pressure. In the entropy change graph given as a function of temperature (Fig. 6c), entropy increased with temperature and decreased with pressure. In Fig. 6d, where the variation of heat capacity with temperature and pressure is shown, the heat capacity, which was zero at absolute temperature, increased rapidly with the increase in temperature and reached the Dulong-Petit [49] limit value of approximately 250 K. At ambient pressure, the heat capacity reaches approximately 96 J/(K mol) at high temperatures. At low temperatures, the electronic heat capacity can be neglected as it is very small compared to the cage heat capacity [50]. As seen in Fig. 6d, the heat capacity decreased with increasing pressure. This is because the knitting parameter decreases with increasing pressure. The reduction of the knitting parameter resulted in low vibration energy and low heat capacity.

4. Conclusion

In this research, we conducted a comprehensive analysis of the structural, elastic, and thermodynamic properties of ternary magnesium alloys called $MgXY_2$ using first-principles calculations. The equilibrium lattice constants obtained from our simulations showed excellent agreement with previously published data. This consistency reinforces the reliability of our study. Furthermore, we proposed empirical relationships to estimate both the lattice constant and the elastic modulus at specified intermediate pressure levels.

Our calculations revealed that $MgXY_2$ alloys remain stable without undergoing any phase transitions within the pressure range of 0–500 kBar. We also calculated three independent elastic constants and found that these alloys exhibit mechanical stability within the same pressure range. The analysis of elastic modulus alongside the first derivative of bulk modulus indicated that these materials do not experience sudden hardening under applied stress conditions. Additionally, Vickers hardness assessments confirmed their classification as soft materials. Based on G/B ratios, Poisson's ratio (ϑ), and heat capacity (C_p) values, it was determined that $MgXY_2$ alloys possess ductile characteristics suitable for various applications.

A thorough anisotropy analysis further established that these alloys exhibit significant anisotropic behavior in their mechanical properties. Moreover, we calculated crucial thermodynamic parameters such as Debye temperature and melting temperature alongside determining a theoretical minimum for thermal conductivity for these materials. We explored free energy changes, vibrational energy contributions, entropy variations, and heat capacity over a temperature spectrum ranging from 0 to 800 K to gain deeper insights into their thermal behavior under different conditions. Ultimately, our findings suggest that $MgXY_2$ alloys are promising candidates for use in high-temperature applications as thermal barrier coatings (materials like biomedical applications) due to their mechanical stability at pressures up to 500 kBar combined with anisotropic and ductile characteristics (materials for underwater vehicles).

Declaration of competing interest

The authors declare that they have no known competing financial interests or personal relationships that could have appeared to influence the work reported in this paper.

CRediT authorship contribution statement

Tahsin Özer: Data curation, Conceptualization. **Murat Çanlı:** Writing – review & editing, Writing – original draft.

Nihat Arıkan: Software, Methodology. **Ali İhsan Öztürk:** Visualization, Investigation.

Acknowledgments

The computational resources used in this study were provided with the support of the National Center for High Performance Computing (UHeM) #1012332022#.

References

[1] J. He, K. Li, T. Wu, J. Chen, S. Li, X. Zhang, MedComm–Biomater. Appl. 2 (4) (2023) 1–32, doi:10.1002/mba2.60.
[2] K.K. Thomas, M.N. Zafar, W.G. Pitt, G.A. Husseini, Appl. Sci. 14 (1) (2023) 10.
[3] J.L. Wang, J.K. Xu, C. Hopkins, D.H.K. Chow, L. Qin, Adv. Sci. 7 (8) (2020) 1902443.
[4] F.Z. Akbarzadeh, M. Sarraf, E.R. Ghomi, V.V. Kumar, M. Salehi, S. Ramakrishna, S. Bae, J. Magnes. Alloys 12 (7) (2024) 2569–2594.
[5] V. Tsakiris, C. Tardei, F.M. Clicinschi, J. Magnes. Alloys 9 (6) (2021) 1884–1905.
[6] F. Xing, S. Li, D. Yin, J. Xie, P.M. Rommens, Z. Xiang, ... U. Ritz, J. Magnes. Alloys 10 (6) (2022) 1428–1456.
[7] A. Babenko, E. Ghasali, S. Raza, K. Baghchesaraee, Y. Cheng, A. Hayat, P. Liu, S. Zhao, Y. Orooji, J. Magnes. Alloys 12 (4) (2024) 1311–1345.
[8] X. Li, Z. Yuan, C. Liu, Y. Sui, T. Zhai, Z. Hou, ... Y. Zhang, Int. J. Hydrogen Energy 50 (2024) 1401–1417.
[9] J. Jiang, X. Geng, X. Zhang, J. Magnes. Alloys 11 (6) (2023) 1906–1930.
[10] D. Kumar, R.K. Phanden, L. Thakur, Mater. Today: Proc. 38 (2021) 359–364.
[11] B. Shi, J. Xu, J. Zou, Y.R. Li, Z. Zhou, K. Liu, H.B. Jiang, Heliyon 10 (4) (2024) 1-43.
[12] N. Arikan, S. Al, A. Iyigör, J. Molec. Model. 28 (2022) 366, doi:10.1007/s00894-022-05358-7.
[13] J.M. Meier, J. Caris, A.A. Luo, J. Magnes. Alloys 10 (6) (2022) 1401–1427.
[14] J. Yang, X. Wang, M.R. Khan, G.A. Hammouda, P. Alam, L. Meng, W. Zhang, Sustain. Mater. Technol. 40 (2024) 1–13.
[15] T. Nadjia, L. Beldi, A. Mohammed, A. Ibrahim, B.L. Farah, Y. Al-Douri, ... R.A. Al-Samarai, Chem. Africa 7 (3) (2024) 1619–1628.
[16] H. Missoum, K. Talbi, F. Khelfaoui, B. Bouhadef, A. Mir, Y. Cherchab, ... Y. Al-Douri, J. Phys. Chem. Solids 193 (2024) 112186.
[17] F. Belkharroubi, W. Belkilali, F. Khelfaoui, F. Boudahri, M. Zahraoui, N. Belmiloud, ... Y. Al-Douri, Crystal Res. Technol. 59 (1) (2024) 2300238.
[18] P. Giannozzi, O. Baseggio, P. Bonfà, D. Brunato, R. Car, I. Carnimeo, ... S. Baroni, J. Chemical Phys. 152 (15) (2020) 154105, doi:10.1063/5.0005082.
[19] J.P. Perdew, K. Burke, M. Ernzerhof, Phys. Rev. Letters 77 (18) (1996) 3865, doi:10.1103/PhysRevLett.77.3865.
[20] D. Vanderbilt, Physic. Rev. B 41 (11) (1990) 7892–7895, doi:10.1103/PhysRevB.41.7892.
[21] J.W. Wafula, J.W. Makokha, G.S. Manyali, Results in Phys. 43 (2022) 106132.
[22] A. Batool, Y. Zhu, X. Ma, M.I. Saleem, C. Cao, Appl. Surface Sci. Adv. 11 (2022) 100275.
[23] T.H. Fischer, J. Almlöf, J. Phys. Chem. 96 (24) (1992) 9768–9774, doi:10.1021/j100203a036.
[24] A. Jain, S.P. Ong, G. Hautier, W. Chen, W.D. Richards, S. Dacek, S. Cholia, D. Gunter, D. Skinner, G. Ceder, K.A. Persson, APL Mater. 1 (1) (2013) 011002, doi:10.1063/1.4812323.
[25] S. Kirklin, J.E. Saal, B. Meredig, A. Thompson, J.W. Doak, M. Aykol, S. Rühl, C. Wolverton, NPJ Computat. Mater. 1 (1) (2015) 15010, doi:10.1038/npjcompumats.2015.10.
[26] J.E. Saal, S. Kirklin, M. Aykol, B. Meredig, C. Wolverton, JOM 65 (11) (2013) 1501–1509, doi:10.1007/s11837-013-0755-4.
[27] N. Arıkan, O. Örnek, Z. Charifi, H. Baaziz, Ş. Uğur, G. Uğur, J. Phys. Chem. Solids 96-97 (2016) 121-12, doi:10.1016/j.jpcs.2016.05.009.
[28] Y.H. Duan, Y. Sun, M.J. Peng, S.G. Zhou, J. Alloys Comp. 585 (2014) 587–593, doi:10.1016/j.jallcom.2013.09.211.
[29] E.S. Yousef, A. El-Adawy, N. El-KheshKhany, Solid State Commun. 139 (3) (2006) 108–113, doi:10.1016/J.SSC.2006.05.022.
[30] Y. Tian, B. Xu, Z. Zhao, Int. J. Refract. Met. Hard Mater. 33 (2012) 93–106, doi:10.1016/J.IJRMHM.2012.02.021.
[31] A. Iyigör, S. Al, N. Arikan, Chem. Phys. Letters 806 (2022) 140052, doi:10.1016/j.cplett.2022.140052.
[32] F. Xue, J. Wang, X. Liu, X. Sun, Optik (Stuttg) 232 (2021) 166533, doi:10.1016/j.ijleo.2021.166533.
[33] S. Sharma, D.C. Gupta, Inorganic Chem. Commun. 172 (2025) 1–20 113466.
[34] R. Li, Q. Shao, E. Gao, Z. Liu, Extreme Mechan. Letters 34 (2020) 100615.
[35] T.W. Heo, S.A. Khairallah, R. Shi, J. Berry, A. Perron, N.P. Calta, ... M.J. Matthews, J. Phys.: Mater. 4 (3) (2021) 034012.
[36] G. Kadim, R. Masrour, Ceram. Int. 51 (1) (2024) 147–153.
[37] R. Gaillac, P. Pullumbi, F.-X. Coudert, J. Phys. 28 (27) (2016) 275201, doi:10.1088/0953-8984/28/27/275201.
[38] K.W. Böer, U.W. Pohl, in: Semiconductor Physics, Springer International Publishing, Cham, 2023, pp. 113–155.
[39] Y.H. Duan, Y. Sun, M.J. Peng, S.G. Zhou, J. Alloys Compd. 595 (2014) 14–21, doi:10.1016/j.jallcom.2014.01.108.
[40] W.A. Wakeham, M.J. Assael, Mechanical Variables Measurement-Solid, Fluid, and Thermal, CRC Press, 2023 14-1.
[41] F. Arab, F.A. Sahraoui, K. Haddadi, A. Bouhemadou, L. Louail, Phase Transit. 89 (5) (2016) 480–513, doi:10.1080/01411594.2015.1089574.
[42] D.G. Cahill, S.K. Watson, R.O. Pohl, Phys. Rev. B 46 (10) (1992) 6131, doi:10.1103/PhysRevB.46.6131.
[43] D.R. Clarke, Surface Coat. Technol. 163–164 (2003) 67–74, doi:10.1016/S0257-8972(02)00593-5.
[44] J. Kou, Y. Zhou, K.-L. Li, L.-H. Gan, Computat. Mater. Sci. 182 (2020) 109758, doi:10.1016/j.commatsci.2020.109758.
[45] C.M.I. Okoye, Computat. Mater. Sci. 92 (2014) 141–148, doi:10.1016/j.commatsci.2014.05.016.
[46] Y. Sun, A. Yang, Y. Duan, L. Shen, M. Peng, H. Qi, Int. J. Refract. Met. Hard Mater. 103 (2022) 105781, doi:10.1016/j.ijrmhm.2022.105781.
[47] M.E. Fine, L.D. Brown, H.L. Marcus, Scripta Metall. 18 (9) (1984) 951–956, doi:10.1016/0036-9748(84)90267-9.
[48] T. Özer, in: H. Demirkaya, M. Canbulat, A. Pulur, M. Eraslan, B. Direkci (Eds.), 4 th International Congress on Multidisciplinary Studies, 2018, pp. 87–99.
[49] I. Chebbab, F. Chiker, N. Baki, R. Miloua, Y.A. Khachai, H. Khachai, ... G. Surucu, Optic. Quantum Electron. 56 (8) (2024) 1299.
[50] K. Vishwanathan, M. Springborg, J. Mater. Sci. Eng. 6 (2017) 325.